Long-Term Trends in Marine Boundary Layer Properties over the Atlantic Ocean

Juan P. Díaz, Francisco J. Expósito, Juan C. Pérez, and Albano González

Grupo de Observación de la Tierra y de la Atmósfera, Universidad de La Laguna, La Laguna, Tenerife, Spain

Yuqing Wang

International Pacific Research Center and Department of Atmospheric Sciences, School of Ocean and Earth Science and Technology, University of Hawai'i at Mānoa, Honolulu, Hawaii

Leopold Haimberger

Department of Meteorology and Geophysics, University of Vienna, Vienna, Austria

Junhong Wang

New York State Mesonet, State University of New York at Albany, Albany, New York

ABSTRACT

The marine boundary layer (MBL) is a key component of Earth's climate system, and its main characteristics (height, entrainment efficiency, energy and mass fluxes, cloud formation processes, etc.) are closely linked to the properties of the inversion layer, which generally determines its height. Furthermore, cloud response to a warmer climate, one of the main sources of uncertainty in future climate projections, is highly dependent on changes in the MBL and in the inversion-layer properties. Long-term trends of the time series of MBL parameters at 32 stations in the Atlantic Ocean have been analyzed using conveniently homogenized radiosonde profiles from 1981 to 2010. In general, decreasing trends are found in the strength and thickness of the inversion layer and in the difference between the precipitable water vapor (PWV) in the free troposphere and the MBL. In contrast, positive trends are found in the height of the bottom of the inversion layer, the lapse rates of virtual and equivalent potential temperatures, the PWV within the boundary layer, and the sea surface temperature (SST). The weakening trend of the inversion layer and the increasing desiccation of the free troposphere relative to the MBL could have important consequences for both the evolution of low cloud cover in a greenhouse-warming climate and the fragile local ecosystems, such as "cloud forests."

1. Introduction

The planetary boundary layer (PBL) is the part of the atmosphere closest to Earth's surface and thereby is directly influenced by the surface–atmosphere exchanges of momentum, moisture, energy, and pollutants. The PBL processes are also of primary importance for realistic modeling of cloud properties (Medeiros et al. 2005).

To determine the top of the PBL it is common to study abrupt changes in the vertical gradients of some variables (temperature, humidity, turbulence, wind, etc.), either separately or combining some of them (Chan and Wood 2013). Many methods exist to measure these gradients based on data obtained from both surface and spaceborne remote sensors: radiosondes, aircraft, wind profilers, lidar, and GPS radio occultation techniques (Zhang et al. 2012; Molod et al. 2015). The study of the PBL using satellite remote sensing techniques is especially interesting since it offers the possibility of carrying out studies of the properties of this layer for the whole planet. However, substantial differences have been observed among the existing retrieval methods (Wang and Wang 2014). The results show that the estimated PBL depth depends upon the definition used and the instrumentation and algorithms adopted in retrievals

Corresponding author address: Juan P. Díaz, jpdiaz@ull.es

(McGrath-Spangler and Denning 2013). Most of the differences are usually associated with the inconsistencies of the temperature and humidity profiles when the boundary layer is not well mixed, or with errors measuring the specific humidity and reflectivity, mainly within clouds (Wang and Wang 2014). Seidel et al. (2010) evaluated seven automated algorithms based on different PBL definitions to a radiosonde dataset and suggested several optimal methods for obtaining robust global climatologies of the PBL height. Moreover, von Engeln and Teixeira (2013) found that the method based on the gradient of relative humidity (RH) provides a robust way to determine the height of the cloudy boundary layer. Cao et al. (2007) studied the thermal inversion layer in the Hawaiian trade wind regime based on both the vertical temperature gradient and vertical profile of RH, as also done by Zhang et al. (2016a,b) in their present and future climate simulations for the Hawaiian region.

Our main interest here is to study the PBL properties over the Atlantic Ocean, namely the marine boundary layer (MBL), because of its importance to boundary layer cloud processes. The MBL over the subtropical oceans is characterized by the temperature inversion cap with convective processes underneath sometimes promoting overshooting thermals penetrating into the inversion layer (Wang et al. 2004a,b). This often results in extensive areas of marine stratocumulus and shallow cumulus clouds. Stratocumulus clouds frequently occur over subtropical eastern oceans with enormous area coverage. From the subtropics to the equator, a cloud regime transition typically occurs, by which the stratocumulus cloud layer slowly thins, then breaks up, and finally is dominated by cumulus clouds, which have a much lower cloud fraction and reflect less sunlight than stratocumulus clouds (Wang et al. 2011). Therefore, cloud regime transition causes a decrease of the cloud-induced net cooling effect to Earth's climate system and its realistic simulation is particularly important, while also quite challenging to climate models (Zhang et al. 2011). Special attention needs to be given to regions where the stratocumulus clouds are quasi-permanent, in particular the regions influenced by trade winds in the tropics and subtropics, where the temperature inversion is a fundamental climate feature (Klein and Hartmann 1993). Most of the tropical–subtropical regions are affected by subsidence associated with the overturning airflow driven by rising motion in the intertropical convergence zone (ITCZ), which only covers a small percentage of the tropical regions, while the cloud-top cooling could further enhance the ITCZ convection (Wang et al. 2005). The trade wind inversion (TWI) is produced by the interaction of this large-scale subsiding air and the convective and turbulent air below (Wood 2012).

The influence of tropical–subtropical low clouds on the energy budget of the climate system has been widely studied and recognized as a key source of uncertainties in cloud–climate feedbacks in climate change simulations (Nam et al. 2012). During the past decades, considerable efforts have been devoted to addressing questions about the processes controlling the space–time distribution of low clouds in the present climate and in a greenhouse-induced warming climate (Bretherton and Blossey 2014; Lauer et al. 2010, 2012). The equilibrium climate sensitivity, evaluated from climate models, ranges between 1.5° and 5.0°C for a doubling of atmospheric carbon dioxide concentration. The large range in climate sensitivity is explained in part by the uncertainty associated with different feedbacks related to low clouds (Lauer et al. 2010). About 50% of the variance in climate sensitivity can be explained by differences in the simulated strength of convective mixing between the lower and middle tropical troposphere (Sherwood et al. 2014). In general, the cloud changes in the subsidence regions are determined roughly by the competition between convective drying and turbulent moistening of the MBL (Demoto et al. 2013). Some of the model-predicted responses of low clouds in regions of strong subsidence and temperature inversion have been corroborated experimentally (Myers and Norris 2013).

From a local point of view, among the ecosystems that could be affected by changes in the MBL and in the low-cloud properties, the "cloud forests" are remarkable, namely those ecosystems closely associated with boundary layer clouds. One of the zones where these ecosystems are of outstanding biological, socioeconomical, and hydrological value is the Macaronesian region (the Azores, Madeira, the Canary Islands, and Cape Verde; Sperling et al. 2004). The forest belt in these archipelagos is highly sensitive to regional change in climate conditions and some authors point to a shift in the lower ecotone for this type of forest on islands (Pouteau et al. 2018) due to climate change.

The main objective of this work is to establish, based on observational data analysis, the long-term trends of the main properties of the MBL in the Atlantic, focusing on changes that could affect cloud formation. The rest of the paper is organized as follows: Section 2 describes the data and methodology used in this study, the results are then discussed in section 3, and finally the main findings and a brief discussion are given in the section 4.

2. Description of the databases and methodology

To evaluate the vertical profiles of temperature and humidity and to estimate the main properties of the

MBL—inversion strength and thickness, precipitable water vapor (PWV) differences between the free troposphere and the MBL, heights of the base and top of the inversion layer, and so on—the Integrated Global Radiosonde Archive (IGRA), maintained by the NOAA National Centers for Environmental Information, has been used. This database consists of quality-controlled radiosonde and pilot balloon observations at over 2700 stations around the world, with records spanning as long as 60 years (Durre et al. 2006). The parameters included in the IGRA-derived dataset can be grouped into three categories: observed variables, basically derived quantities, and vertical gradients. They are available for standard, surface, tropopause, and significant levels at which the sounding deviates from linearity (in the logarithm of pressure) between two standard levels. Therefore, the inversion layer can be quite accurately captured in the radiosonde data. The derived dataset, version 2 (Durre and Yin 2008), includes pressure, temperature, geopotential height, dewpoint depression, wind direction, and wind speed. The vertical resolution in the IGRA records has been improved significantly since 1950. The data are currently provided with an average number of more than 35 levels for the entire sounding, with around 5 levels between the surface and 850 hPa and around 10 levels in the 300–70-hPa layer. Therefore, the temporal and spatial coverages and the fully automated quality-assurance (QA) procedures applied to the IGRA provide an excellent opportunity for studying the long-term variability of those characteristics in the MBL (Durre et al. 2008).

However, long-term data in the IGRA have some discontinuities mainly due to changes in instruments, procedures, and station relocations (Haimberger et al. 2008; Wang et al. 2013). Some homogenization methods are attempted to correct these problems, especially at mandatory pressure levels for temperature, humidity, or wind speed. In particular, to homogenize the IGRA temperature records, we have used the method of Haimberger et al. (2008, 2012). These authors proposed a method called Radiosonde Innovation Composite Homogenization (RICH), which uses the breakpoint data information from the Radiosonde Observation Correction Using Reanalyses (RAOBCORE) method (Haimberger 2007) to determine homogeneous pieces of radiosonde time series, which are used for break-size estimation in our study. The references for break-size estimation are composites of homogeneous pieces of temperature time series from neighboring radiosonde stations. Haimberger et al. (2008) demonstrated that the RICH methods could remove most of the global mean cooling bias of radiosonde temperatures compared to the satellite data and that the temperature trends from the RICH–RAOBCORE

(version 1.4) are more consistent with trends from climate simulations than earlier radiosonde datasets. In addition, these global characteristics of the homogenized datasets also make them useful as input for climate data–assimilation efforts.

The use of radiosonde humidity records also presents difficulties because of discontinuities and changes in the operational programs (instrumentation, observing protocols, etc.). In addition, these radiosonde records need to be homogenized before they can be used to estimate long-term humidity and derived variable trends. In particular, the IGRA humidity records, up to 100 hPa in height, were homogenized by Dai et al. (2011) using an algorithm based on two statistical tests: the Kolmogorov–Smirnov (K–S) test and the maximal penalized F test (PMFred). The first test searches for changes in distributions and the second one detects mean shifts in the occurrence frequency for different bins of dewpoint depression. The new homogenized data show only small changes in RH in the lower and middle troposphere and exhibit more coherent trends than the raw data. When homogenized dewpoint depression records are combined with homogenized radiosonde temperature, other atmospheric humidity variables can be calculated accordingly. Furthermore, the adjusted estimates show an increase in tropospheric water vapor globally (Wang et al. 2013; Dai et al. 2011). The homogenized humidity data have been used to study global long-term precipitable water trends (Wang et al. 2016). The PWV values were computed as the integral of water vapor density from the surface to the thermal inversion altitude for the MBL layer (WVB) and from the MBL to the top height of the radiosonde for the free-troposphere layer (WVF).

The above homogenization methods allow us to correct the temperature and humidity data only at the mandatory pressure levels of the radiosonde. Because of the vertical resolution required to obtain the TWI, all the rest of the levels of the radiosonde, mainly in the lower altitudes, are used. To homogenize these data, pressure-weighted corrections for each point between two mandatory levels with known homogenization factors were introduced. This procedure homogenizes all standard and significant points and, therefore, improves the accuracy of the reconstruction of the vertical profile without sacrificing vertical resolution to properly obtain the thermal inversion layer. Figure 1 shows an example of the homogenization in a vertical radiosonde profile.

To study the long-term trends of the MBL properties over the Atlantic Ocean, a 30-yr period, from 1981 to 2010, has been chosen, with homogenized temperature and humidity records from radiosondes of 32 stations
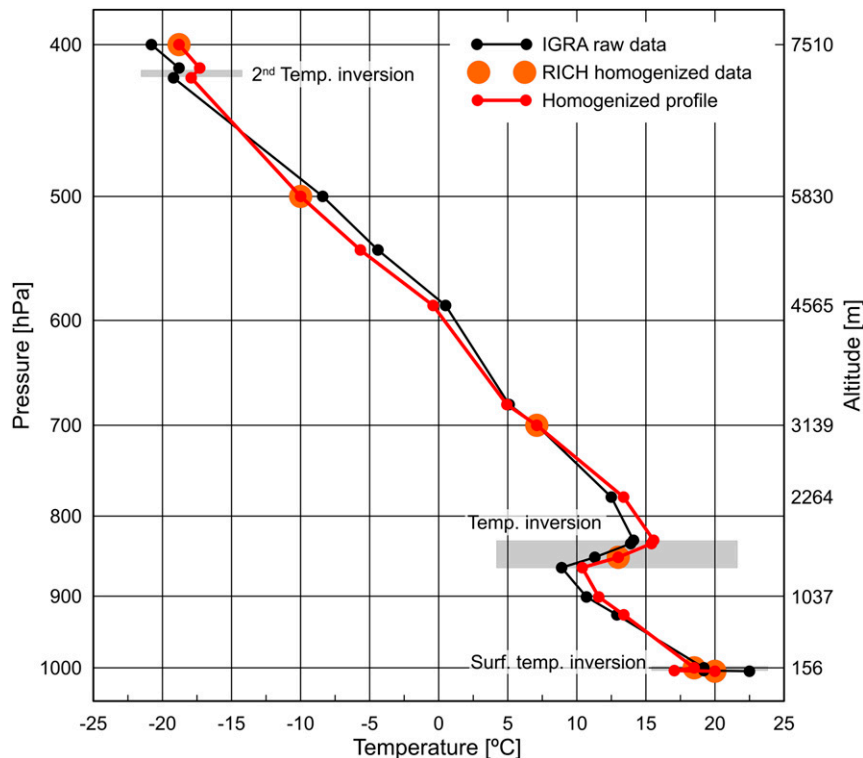
FIG. 1. Example of a profile homogenization using RICH data.

(Fig. 2) distributed from the Azores (~40°N) to Gough Island (~40°S).

The monthly averaged properties of the thermal inversions for each station are only computed for those months for which at least 10 radiosonde profiles are available. This requirement reduces the total number of monthly mean data. Thus, on average, for the whole period and all stations, 27% of months were not used in the analyses. Table 1 indicates the total number of analyzed radiosonde profiles and the percentage of cases for which a temperature inversion was detected. The results were classified according to their latitude.

The MBL top is identified from the homogenized IGRA temperature and humidity database following the criteria given by Cao et al. (2007), with some adjustments for particular conditions of the Atlantic region and explained below:

1) Initially, the base and top of all possible temperature inversions are identified as those points of the radiosounding at which a change in the sign of the vertical temperature gradient is found (from negative to positive for the base, and from positive to negative for the top). Those inversions with base height below 350 m, top pressure below 400 hPa, or temperatures below 273 K are discarded to exclude surface

radiative inversions or inversions whose formation mechanism is different from that of the MBL, such as those due to processes of the ice particles melting (Johnson et al. 1996).

2) In case of several inversions detected in the same radiosounding from the previous step, the top of the MBL is identified as the layer across which the maximum rate of decrease of RH with height is found.

3) The selected inversion is checked to eliminate spurious superadiabatic layers, appearing in temperature records in the base of the inversion layer. These situations are an artifact caused by the rapid evaporation of moisture in the temperature sensor when it leaves a cloud and starts to ascend into a dry layer, which cools the temperature of the sensor below the ambient air temperature.

Seidel et al. (2010) found that, depending on the method, the PBL height estimates could be sensitive to the vertical resolution of the radiosondes: statistically significant higher PBL were estimated using standard sounding versus high-vertical-resolution sounding data. They also concluded that the best results, although statistically insignificant on the PBL estimations (at about half of the stations analyzed), are obtained using the minimum gradient of RH or the maximum vertical
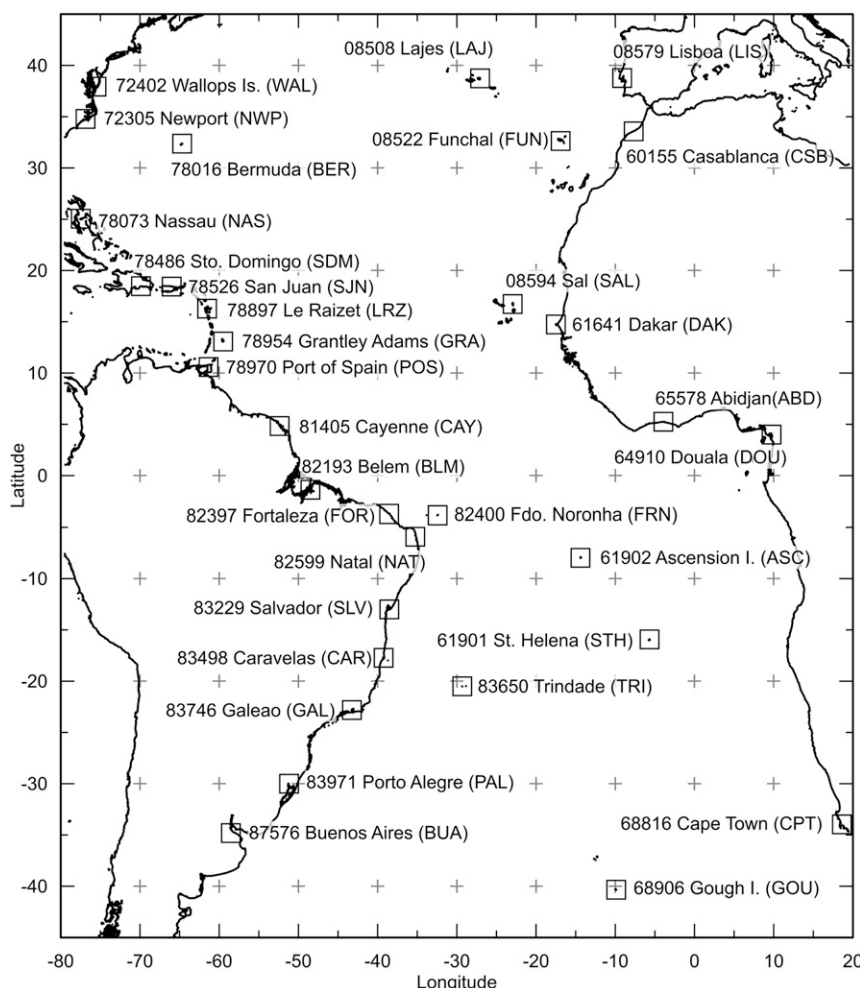
FIG. 2. Stations chosen for this study with their WMO code, name, and the acronym used throughout the study.

gradient of potential temperature. Therefore, in this study, for IGRA profiles of radiosondes, to diminish the possible influence of the vertical resolution in the data on the PBL estimations, the second condition that was imposed in the process to identify the PBL is based on the maximum rate of RH decrease.

The systematic use of the above criteria yields the following MBL long-term variables for each station: bottom and top altitudes of the inversion layer (BIL and TIL, respectively), thickness (THK, defined as TIL − BIL), and PWV in the MBL (WVB) and from this height to the top altitude reached by the radiosonde around 100 hPa, a layer that we consider as the free troposphere (WVF) above the inversion layer. Although not all radiosondes reach the same altitude, the contribution of PWV at high altitudes is negligible compared to the total amount. From these data, it was found that the amount of water vapor above 300 hPa in the atmosphere is less

than 5% of that in the free-troposphere layer. Several authors have found a strong linkage between the low-cloud fraction and the stability of the lower troposphere, closely related to the strength of the thermal inversion (Slingo 1987; Zhang et al. 2009). Klein and Hartmann (1993) introduced the lower-tropospheric stability (LTS), defined as the difference in potential temperature between 700-hPa and the surface, which is highly correlated with the subtropical low-cloud fraction

TABLE 1. Number of radiosonde profiles analyzed and temperature inversions (TI) detected.

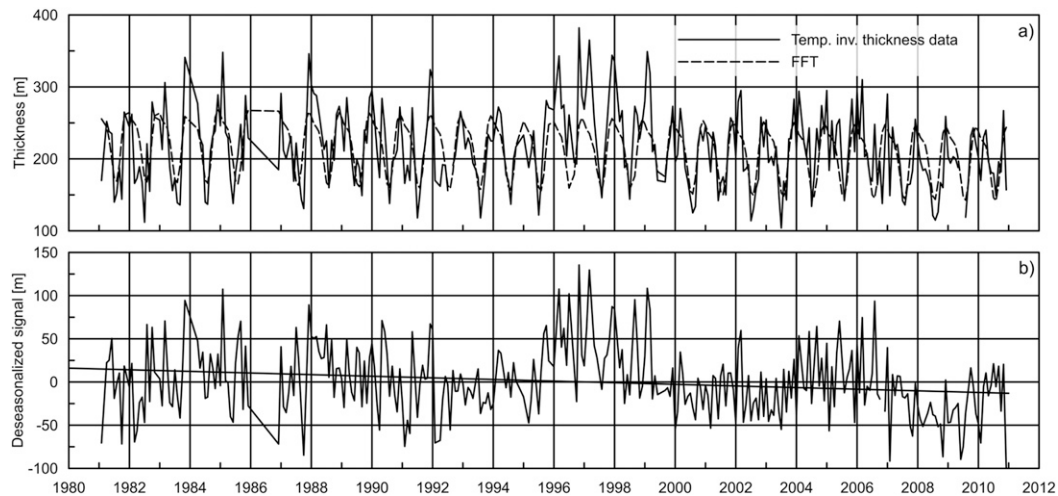| Lat range	No. of profiles	No. of TI
lat > 20°N	119 914	57 716 (48%)
20°N ≥ lat ≥ 20°S	203 377	95 461 (47%)
lat < 20°S	94 154	49 002 (52%)
Total	417 445	202 179 (48%)

FIG. 3. Temperature inversion thickness at the Bermuda station (BER): (a) raw data and seasonality and (b) deseasonalized series and computed linear trend.

on a seasonal time scale. Wood and Bretherton (2006) proposed a bulk measure of inversion stability in terms of the estimated inversion strength (EIS) parameter, which is a more regime-independent predictor of stratus cloud fraction than the LTS and improves the correlations with the cloud fraction under a wide range of climatological conditions. Because of this close relationship between inversion strength and low-cloud fraction, in this work, the strength of the inversion layer was also evaluated. However, instead of using the previous approximations, the strength of the inversion layer (SIL) was directly evaluated as the potential virtual temperature at the TIL minus the potential temperature at the BIL from the radiosonde vertical profiles.

To facilitate the interpretation of the long-term trends in the MBL main properties, three ancillary datasets were also analyzed: the sea surface temperature (SST) and the vertical pressure velocity ω from ERA-Interim (Dee et al. 2011), and the International Satellite Cloud Climatology Project (ISCCP) data for low-cloud cover (Rossow and Schiffer 1999). The ERA-Interim data are gridded with $0.75° \times 0.75°$ horizontal resolution and 32 vertical pressure levels (for the case of pressure velocity) at 6-h intervals and available since 1979. This reanalysis has been widely evaluated against other reanalysis and measurements in both global and regional climate studies, showing an excellent representation of main climate variables (Decker et al. 2012). Regarding the ISCCP data, we used the monthly mean of low cloud cover for the period 1984–2001. These data have a spatial resolution of $2.5° \times 2.5°$ and provide cloud cover at three layers, corresponding to low, middle, and high clouds.

The long-term trends are frequently modulated by annual and semiannual cycles, so in order to increase the accuracy in the trend evaluation, it is convenient to remove the main harmonic signals in the time series. To select the frequencies (annual, semiannual, or no frequencies) to be removed we applied a continuous wavelet transform (CWT) procedure based on Torrence and Compo (1998). Following Cao et al. (2007), the global wavelet spectrum was compared against the red-noise spectrum to obtain the significant frequencies because of the autoregressive nature of the atmospheric time series. Following this, once these frequencies were removed, the linear trends of all selected variables were evaluated. To account for the autocorrelation behavior of geophysical variables, a first-order autocorrelation (lag 1) was assumed and a generalized least squares fit with autocorrelated first-order autoregressive [AR(1)] errors was applied (Montgomery et al. 2012). As an example, Fig. 3 shows the procedure used to evaluate the trend in the thickness of the temperature inversion layer at the Bermuda station (BER).

3. Results and discussion

The above methodology was applied to the records of 32 radiosonde stations distributed the tropical and subtropical Atlantic Ocean (~40°N to ~40°S) from 1981 to 2010. There were 417 445 radiosonde profiles analyzed; among them 202 179 show at least one valid thermal inversion (48%; see Table 1), indicating the persistence of the thermal inversion in the Atlantic Ocean. A positive trend in the frequency of occurrence of the thermal inversion for 27 out of the 32 stations was found (only one station shows a downward trend), with an average of 10% decade^{-1}. In a similar way, Cao et al. (2007) also obtained a significant upward trend in the frequency of occurrence of the thermal inversion in the Hawaii area

TABLE 2. Number of radiosonde profiles analyzed for each station; number of thermal inversions (TI) found; long-term trends (decade^{-1}) and the corresponding 95% confidence intervals for the bottom (BIL), thickness (THK), strength (SIL) of the inversion layer; and low-cloud cover (LCC). Boldface text indicates statistically significant trends at the 95% level. The stations are listed from northernmost to southernmost latitude; see Fig. 2 for station locations.

Station	No. of profiles	No. of TI	BIL (m decade^{-1})	THK (m decade^{-1})	SIL (K decade^{-1})	LCC (% decade^{-1})
08579 LISBOA (LIS)	13 302	7931	**+68 ± 25**	**−35.9 ± 4.1**	**−0.373 ± 0.082**	−0.44 ± 0.80
08508 LAJES (LAJ)	15 950	8465	**+48 ± 24**	**−37.3 ± 5.6**	**−0.40 ± 0.12**	−0.2 ± 1.1
72402 WALLOPS IS. (WAL)	21 735	6998	**+54 ± 34**	**−12.2 ± 7.3**	**−0.13 ± 0.11**	−0.10 ± 0.96
72305 NEWPORT (NWP)	21 504	8459	+17 ± 59	**−11.4 ± 6.3**	**−0.15 ± 0.12**	**+1.64 ± 0.87**
60155 CASABLANCA (CSB)	7571	4821	+41 ± 51	**−48 ± 10**	**−0.63 ± 0.23**	**−1.61 ± 0.67**
08522 FUNCHAL (FUN)	12 109	7255	**+93 ± 26**	**−56.1 ± 6.7**	**−0.78 ± 0.12**	**−2.5 ± 1.1**
78016 BERMUDA (BER)	18 331	9282	**+45 ± 29**	**−14.5 ± 5.2**	**−0.136 ± 0.094**	−0.61 ± 0.84
78073 NASSAU (NAS)	9412	4506	**+85 ± 40**	+2.8 ± 7.1	+0.06 ± 0.14	+0.37 ± 0.62
78486 STO DOMINGO (SDM)	10 438	5267	+36 ± 37	**−26.5 ± 6.6**	**−0.33 ± 0.13**	−0.15 ± 0.57
78526 SAN JUAN (SJN)	21 520	15 489	**+35 ± 26**	**−28.0 ± 3.9**	**−0.417 ± 0.081**	**−0.65 ± 0.59**
08594 SAL (SAL)	8550	5065	**+66 ± 40**	**−74.6 ± 9.6**	**−1.18 ± 0.20**	**−1.15 ± 0.68**
78897 LE RAIZET (LRZ)	17 421	6634	−7 ± 40	+1.0 ± 6.2	+0.05 ± 0.10	−0.38 ± 0.60
61641 DAKAR (DAK)	20 644	8484	**+200 ± 47**	**−25.3 ± 7.8**	**−0.33 ± 0.13**	**−1.11 ± 0.55**
78954 G. ADAMS (GRA)	15 367	9336	**+46 ± 33**	**−12.1 ± 5.2**	**−0.194 ± 0.088**	−0.55 ± 0.60
78970 PORT OF SPAIN (POS)	13 900	6285	**+89 ± 47**	**−21.3 ± 5.2**	**−0.364 ± 0.084**	−0.44 ± 0.58
65578 ABIDJAN (ABD)	14 135	3368	**+241 ± 88**	**−44 ± 12**	**−0.47 ± 0.14**	+0.16 ± 0.48
81405 CAYENNE (CAY)	16 208	3612	−23 ± 151	−7 ± 15	−0.15 ± 0.24	+0.44 ± 0.53
64910 DOUALA (DOU)	10 496	2496	+99 ± 99	**−36.0 ± 8.1**	**−0.42 ± 0.12**	**−0.64 ± 0.59**
82193 BELEM (BLM)	12 542	4869	**+96 ± 62**	**−45.4 ± 5.2**	**−0.531 ± 0.071**	**+1.33 ± 0.42**
82397 FORTALEZA (FOR)	6211	3402	**+85 ± 63**	**−57.8 ± 9.6**	**−0.64 ± 0.13**	+0.67 ± 0.68
82400 FDO NORONHA (FRN)	4527	2067	+80 ± 108	−21 ± 12	−0.21 ± 0.19	**−2.11 ± 0.91**
82599 NATAL (NAT)	7356	4034	+4 ± 54	**−54.6 ± 8.5**	**−0.70 ± 0.12**	+0.32 ± 0.64
61902 ASCENSION IS. (ASC)	6006	4560	**+58 ± 33**	+4.0 ± 6.9	−0.08 ± 0.14	−0.88 ± 0.95
83229 SALVADOR (SLV)	4669	2645	**+73 ± 68**	**−33 ± 13**	−0.38 ± 0.26	−0.56 ± 0.77
61901 ST. HELENA (STH)	10 283	6024	−7 ± 30	**−49 ± 20**	**−0.30 ± 0.20**	+0.4 ± 1.1
83498 CARAVELAS (CAR)	3104	1824	−12 ± 120	**−48 ± 18**	**−0.41 ± 0.37**	−0.13 ± 0.76
83650 TRINDADE (TRI)	5925	3421	**+91 ± 71**	**−32 ± 15**	−0.23 ± 0.33	**−2.51 ± 0.94**
83746 GALEAO (GAL)	15 746	8321	**+76 ± 39**	**−28.6 ± 5.1**	**−0.320 ± 0.094**	+0.07 ± 0.54
83971 PORTO ALEGRE (PAL)	15 741	9658	**+39 ± 28**	**−11.5 ± 4.3**	**−0.129 ± 0.072**	**+1.71 ± 0.81**
68816 CAPE TOWN (CPT)	20 175	10 077	+14 ± 23	**−25.9 ± 5.3**	**−0.230 ± 0.087**	+0.58 ± 0.83
87576 BUENOS AIRES (BUA)	16 184	8960	+12 ± 26	**−44.4 ± 4.5**	**−0.522 ± 0.097**	+0.23 ± 0.79
68906 GOUGH (GOU)	20 383	8565	+8 ± 19	**−29.7 ± 7.1**	**−0.31 ± 0.11**	+0.1 ± 1.0

(5% and 10% decade^{-1} for Hilo and Lihu'e, respectively) but with a higher percentage of occurrence (about 82%). More in detail, Table 2 shows the data for each station and the long-term trends (decade^{-1}) and the corresponding 95% confidence level interval for the BIL, THK, and SIL of the MBL and for the low-cloud cover (LCC). One of the main characteristics that can be observed is the positive trend of the BIL, with statistical significance in 19 stations (none of them have a negative trend with statistical significance), ranging from 35 (SJN and PAL) to 241 m decade^{-1} (ABD) (see Fig. 2 for expansions of station acronyms). The BIL highest trend values appear in the tropical area. Y. Zhang et al. (2013) also observed significant increases in PBL daytime heights in all four seasons in Europe. Figure 4 graphically shows the trends of BIL and SST for each station, where the arrows indicate the behavior of the variable.

SST shows a clear positive trend in the last three decades for 85% of the stations with statistical significance, which is more remarkable between 10° and 20°N, in a stripe between the western African and northern South American coasts. Although the increase in SST could be one of the causes for a higher BIL, as a consequence of the increase of sensible and latent heat fluxes over the ocean, other mechanisms must also play important roles, such as the radiative cooling near the cloud top, lower-tropospheric stability, and the MBL mass loss due to cumulus convection (Medeiros et al. 2005). However, only slightly positive and poor statistically significant correlations (0.2–0.4) between BIL and SST were found at those sites on islands but not at those sites on continental coasts.

The THK shows clear negative trends for almost all stations (28 out of 32). The reduction in the THK for
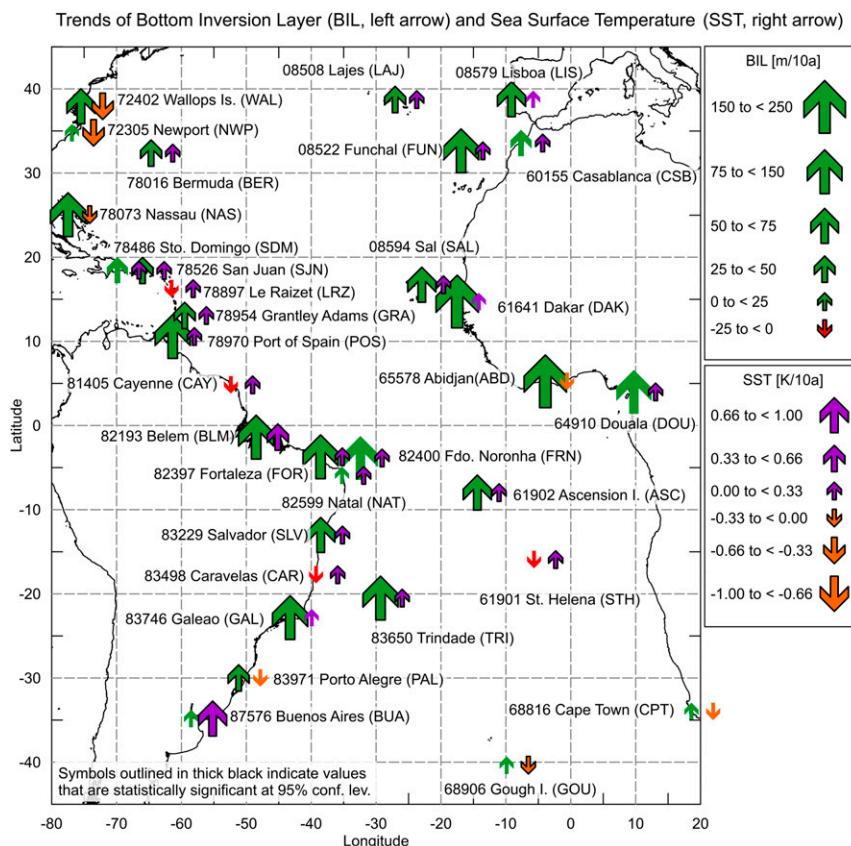
FIG. 4. Trends of the bottom altitude of the inversion layer (BIL; left arrows) and the sea surface temperature (SST; right arrows). Symbols outlined in thick black indicate values that are statistically significant at the 95% confidence level.

statistically significant cases is between −11 (NWP) and −75 m decade^{-1} (SAL). For SIL, the negative trends at 27 stations are statistically significant, and none of the stations show positive trends of statistical significance. The SIL negative trend ranges between −1.2 (SAL) and −0.13 K decade^{-1} (WAL and PAL). Figure 5 depicts the trends of THK and SIL. It can be noted that the negative trends for both variables are less significant in the western Atlantic in the Northern Hemisphere. In summary, both the depth and the strength of the thermal inversion show, in general, a decreasing trend in the Atlantic Ocean, whereas the altitude of the bottom of the thermal inversion and the SST show a general tendency to increase.

It is also important to analyze the variations in the vertical gradient of water vapor. Table 3 shows the long-term trends (decade^{-1}) and the corresponding 95% confidence level for WVF, WVB, and WVD (WVD = WVF − WVB). These parameters are generally characterized by positive trends in WVB (21 stations with statistical significance, none with a negative trend), and negative trends in WVD (statistically significant at 12

stations; none of the 32 stations have positive trends with statistical significance; see Fig. 6). In general, with statistical significance, either the decreasing trend in WVF or the increasing trend has a lower rate than the general increasing trend for WVB (see Table 3). This behavior could be due to an increase in the dry-air subsidence of the Hadley cell. If this is the case, an increase should be found in the vertical motion as reported in some previous studies; for example, Longman et al. (2015) found an increase in vertical motion at 500 hPa in the central tropical North Pacific. To check this possibility for the Atlantic zone the vertical pressure velocity at 500 hPa from ERA-Interim data was examined. The average in a 3° × 3° grid box around each station was calculated. These results show that, with statistical significance in the last three decades, the descending motion (positive vertical pressure velocity) shows increasing trends at only five stations (BER, LRZ, GRA, ABD, and DOU), whereas in three other stations (LAJ, BLM, and ASC) increasing trend in ascending motion is obtained. Given the few stations with statistical significance for vertical movement and disparate trends, the increase in
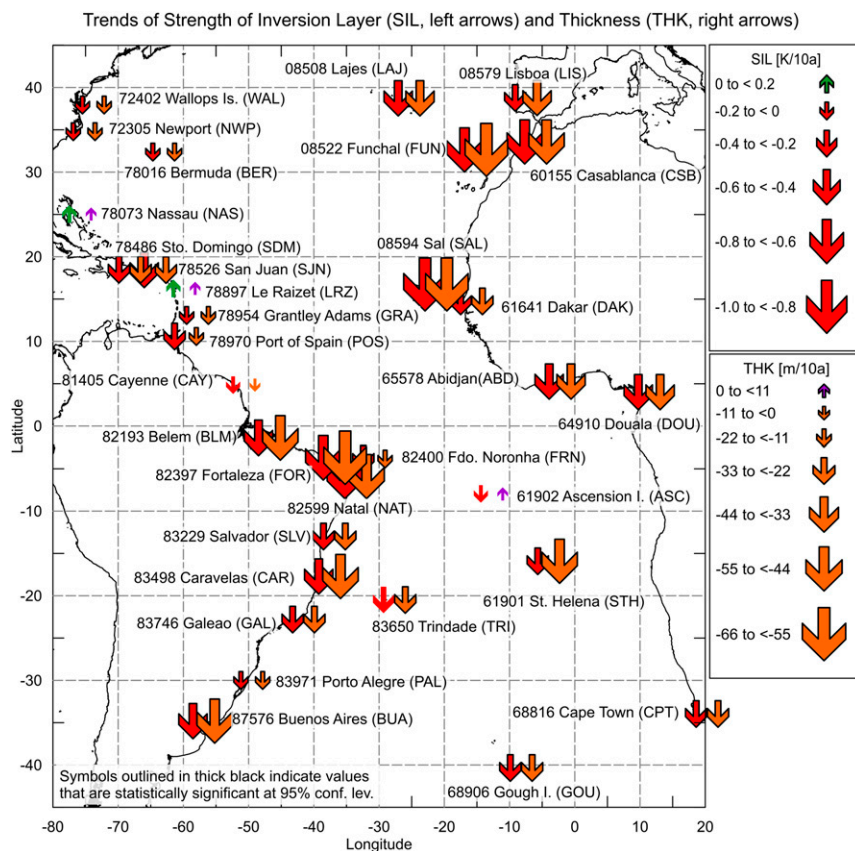
FIG. 5. Trends of the strength of the inversion layer (SIL; left arrows) and thickness (THK; right arrows). Symbols outlined in thick black indicate values that are statistically significant at the 95% confidence level.

downward movement cannot be considered as a primary mechanism for the reduction of PWV in the region.

To study the possible changes in the thermal structure of the MBL, the long-term trends of the lapse rate of potential virtual (LPV) and the lapse rate of saturated equivalent potential temperatures (LPE) were also analyzed (Table 3), both being calculated from the surface to the BIL. They are related to the dry and moist static stability conditions, respectively (Frierson 2006). Figure 7 gives the trend in LPV, which shows a general increasing trend, with 23 stations being statistically significant, and only one station shows a negative trend (STH). This indicates an increase in the static dry stability of the atmosphere, which is consistent with projections in global warming simulations from 21 atmosphere–ocean global circulation models (AOGCMs) in the IPCC Fourth Assessment Report (Frierson 2006). The LPE also exhibits a positive general trend (at 18 stations). In the Northern Hemisphere, only two stations (LRZ and CAY, situated in the western Atlantic) show statistically significant negative trends, whereas only one station (STH) in the eastern South Atlantic shows this behavior.

The changes observed in the inversion properties, including the weakening of the SIL, the thinning of the THK, the increase of the total water vapor in the MBL (WVB), and the possible increase in the differences between water vapor in the MBL and the free troposphere (WVD) provide favorable conditions for the vertical development of clouds. This explains the reduction/destruction of the stratocumulus regime and the formation of cumulus/shallow cumulus clouds with a reduction of cloud cover. Moreover, this also facilitates an increase of the cloud-top dry-air entrainment from the free troposphere (drying and warming the cloud layer), as previously studied using large-eddy simulations (LESs) (Bretherton et al. 2013; Bretherton and Blossey 2014; M. Zhang et al. 2013). The results thus suggest that a projected warmer climate in the future also favors the thinning of the low-cloud layer in the studied region. In general, any change in the entrainment efficiency will adjust to a new equilibrium, also taking into account the radiative cooling, to maintain stratocumulus and shallow cumulus clouds by reducing the in-cloud liquid flux and thus the buoyant generation

TABLE 3. Long-term trends (decade^{-1}) and the corresponding 95% confidence intervals for PWV in the free troposphere (WVF), in the MBL (WVB), differences between the PWV in the free troposphere and in the MBL (WVD), lapse rates of the potential temperature (LPV), and lapse rates of the equivalent potential temperature (LPE). Boldface text indicates statistically significant trends at the 95% level. The stations are listed from northernmost to southernmost latitude; see Fig. 2 for station locations.

Station	WVF (mm decade^{-1})	WVB (mm decade^{-1})	WVD (mm decade^{-1})	LPV (K km^{-1} decade^{-1})	LPE (K km^{-1} decade^{-1})
08579 LISBOA (LIS)	**−0.54 ± 0.19**	**+0.38 ± 0.21**	**−0.91 ± 0.30**	−0.13 ± 0.16	−0.16 ± 0.33
08508 LAJES (LAJ)	**+0.39 ± 0.24**	**+0.36 ± 0.20**	+0.22 ± 0.36	+0.00 ± 0.08	−0.05 ± 0.19
72402 WALLOPS IS. (WAL)	−0.08 ± 0.33	**+0.46 ± 0.32**	−0.40 ± 0.51	**+0.18 ± 0.16**	+0.08 ± 0.29
72305 NEWPORT (NWP)	**+0.90 ± 0.55**	**+1.03 ± 0.72**	−0.11 ± 0.95	+0.06 ± 0.22	+0.03 ± 0.47
60155 CASABLANCA (CSB)	+0.42 ± 0.46	**+0.53 ± 0.36**	−0.12 ± 0.66	**+0.93 ± 0.34**	**+1.84 ± 0.59**
08522 FUNCHAL (FUN)	**−0.57 ± 0.18**	**+0.54 ± 0.23**	**−1.12 ± 0.33**	**+0.39 ± 0.06**	**+0.86 ± 0.61**
78016 BERMUDA (BER)	**+0.52 ± 0.27**	**+0.50 ± 0.27**	+0.14 ± 0.43	**+0.11 ± 0.07**	+0.15 ± 0.18
78073 NASSAU (NAS)	+0.07 ± 0.32	**+0.40 ± 0.44**	−0.11 ± 0.54	**+0.36 ± 0.10**	**+0.91 ± 0.28**
78486 STO DOMINGO (SDM)	−0.12 ± 0.36	−0.20 ± 0.36	+0.04 ± 0.56	**+0.25 ± 0.06**	**+0.86 ± 0.19**
78526 SAN JUAN (SJN)	**+0.37 ± 0.23**	**+0.52 ± 0.25**	−0.09 ± 0.36	**+0.06 ± 0.04**	**+0.18 ± 0.11**
08594 SAL (SAL)	+0.17 ± 0.47	**+0.61 ± 0.36**	−0.29 ± 0.67	**+1.52 ± 0.21**	**+1.87 ± 0.49**
78897 LE RAIZET (LRZ)	−0.26 ± 0.35	+0.16 ± 0.37	−0.46 ± 0.57	−0.02 ± 0.04	**−0.19 ± 0.14**
61641 DAKAR (DAK)	**−1.19 ± 0.46**	**+1.12 ± 0.33**	**−2.37 ± 0.65**	+0.32 ± 0.25	**+0.72 ± 0.49**
78954 G. ADAMS (GRA)	−0.07 ± 0.33	+0.15 ± 0.31	−0.10 ± 0.53	+0.06 ± 0.06	−0.00 ± 0.18
78970 PORT OF SPAIN (POS)	**−0.64 ± 0.45**	**+0.48 ± 0.42**	**−1.14 ± 0.75**	**+0.16 ± 0.06**	**+0.37 ± 0.20**
65578 ABIDJAN (ABD)	−0.66 ± 0.80	**+2.4 ± 1.0**	**−3.2 ± 1.5**	**+0.18 ± 0.09**	**+0.54 ± 0.31**
81405 CAYENNE (CAY)	−0.4 ± 2.0	+0.7 ± 1.8	+1.1 ± 2.3	−0.13 ± 0.20	**−0.65 ± 0.57**
64910 DOUALA (DOU)	+0.2 ± 1.5	**+1.9 ± 1.2**	−1.6 ± 2.7	**+0.18 ± 0.15**	+0.48 ± 0.68
82193 BELEM (BLM)	**−0.91 ± 0.60**	**+2.36 ± 0.62**	**−3.1 ± 1.1**	**+0.21 ± 0.09**	**+0.56 ± 0.29**
82397 FORTALEZA (FOR)	**−0.70 ± 0.59**	−0.58 ± 0.61	−0.5 ± 1.1	**+0.15 ± 0.11**	**+0.46 ± 0.40**
82400 FDO NORONHA (FRN)	+0.54 ± 0.76	**+1.7 ± 1.6**	−0.3 ± 1.5	**+0.40 ± 0.16**	**+0.96 ± 0.68**
82599 NATAL (NAT)	+0.24 ± 0.48	**+0.98 ± 0.46**	**−0.77 ± 0.75**	**+0.15 ± 0.09**	**+0.40 ± 0.31**
61902 ASCENSION IS. (ASC)	**−0.57 ± 0.31**	**+0.52 ± 0.29**	**−1.08 ± 0.52**	+0.08 ± 0.08	+0.20 ± 0.26
83229 SALVADOR (SLV)	+0.53 ± 0.80	+0.57 ± 0.82	+0.2 ± 1.2	**+0.19 ± 0.12**	**+0.64 ± 0.41**
61901 ST. HELENA (STH)	−0.07 ± 0.25	+0.12 ± 0.23	−0.25 ± 0.44	**−0.38 ± 0.09**	**−1.28 ± 0.22**
83498 CARAVELAS (CAR)	+0.5 ± 1.4	+0.9 ± 1.3	−0.6 ± 2.1	−0.04 ± 0.20	−0.01 ± 0.67
83650 TRINDADE (TRI)	**+1.3 ± 1.0**	**+1.00 ± 0.88**	+0.4 ± 1.5	**+0.39 ± 0.15**	**+1.22 ± 0.51**
83746 GALEAO (GAL)	**−0.70 ± 0.50**	**+1.39 ± 0.39**	**−2.15 ± 0.79**	+0.00 ± 0.06	−0.02 ± 0.21
83971 PORTO ALEGRE (PAL)	−0.22 ± 0.32	**+0.27 ± 0.30**	**−0.48 ± 0.48**	+0.14 ± 0.11	**+0.31 ± 0.25**
68816 CAPE TOWN (CPT)	−0.05 ± 0.18	**+0.43 ± 0.17**	**−0.44 ± 0.25**	**+0.37 ± 0.14**	**+1.06 ± 0.27**
87576 BUENOS AIRES (BUA)	**−0.58 ± 0.24**	+0.06 ± 0.26	**−0.58 ± 0.34**	**+0.48 ± 0.11**	**+1.18 ± 0.26**
68906 GOUGH (GOU)	+0.10 ± 0.22	**+0.38 ± 0.16**	−0.24 ± 0.27	+0.00 ± 0.09	−0.06 ± 0.17

of turbulence. This internal cloud-regulating mechanism, which is denominated entrainment liquid-flux adjustment, has been demonstrated by Bretherton et al. (2013). In this regard, the trend in the time series of the ISCCP low-cloud cover (1984–2001) over each station (Table 2) was analyzed. It shows a reduction in this parameter at eight stations and an increase at three sites. The decrease is remarkable in northwest Africa, one of the main areas with permanent stratocumulus cover.

In areas such as the Macaronesian region, the so-called montane cloud forests play a critical role for the inhabitants of these islands because they capture, store, and transport water and thus protect the soils against erosion. Additionally, this ecosystem hosts a high species endemism and biodiversity (Irl et al. 2017), at the same time, being one of the regions that are very sensitive to climate change (Foster 2001). Several studies have reported increases in the lower elevation of the cloud forest along with an increase in temperature and thus the lifting condensation level (LCL), estimated at 4 m °C^{-1} (Pouteau et al. 2018), 50–83 m °C^{-1} (Feeley et al. 2011), 167 m °C^{-1} (Loope and Giambelluca 1998), or even 360 m °C^{-1} (Jump et al. 2012) depending on the region. Moreover, climate model simulations suggest that the future changes in temperature with global warming increase with height over these islands (Expósito et al. 2015). This fact points to a displacement of cloud forest and an increase in the stress of other competitive species that could take advantage of this displacement and occupy the vacant niche. Based on previous discussions about the possible low cloud cover reduction and/or the change in the cloud regime (cumulus/shallow cumulus instead of stratocumulus/stratus), there appears to be a threat to the cloud forest development. The possible reduction in the cloud canopy
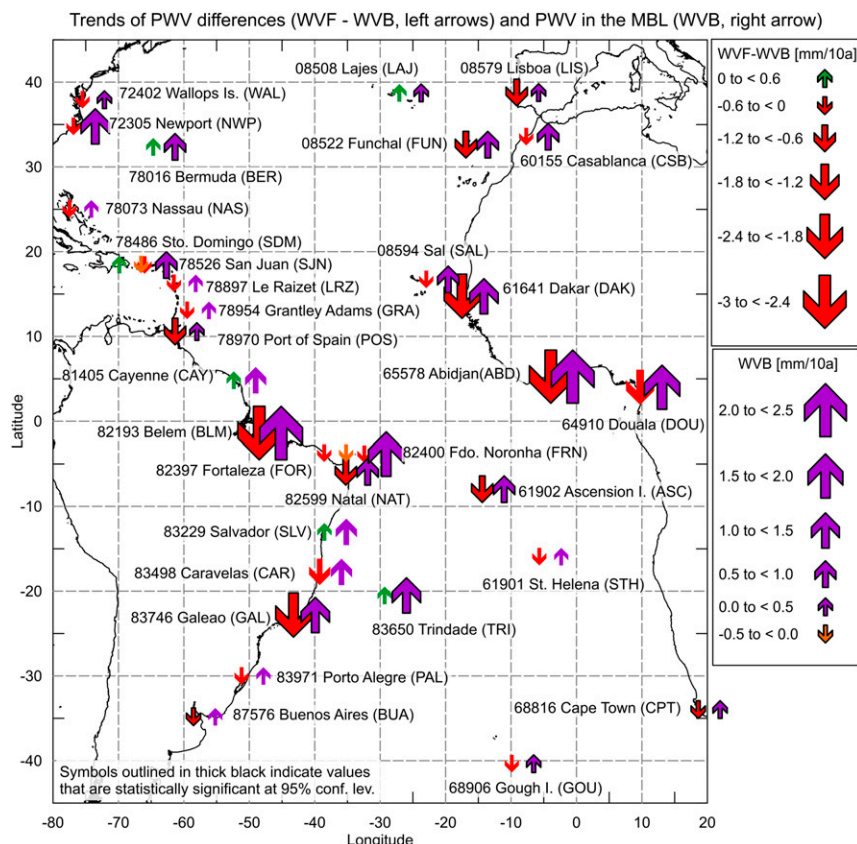
FIG. 6. Trends of the precipitable water vapor differences between the free troposphere and the MBL (WVF − WVB; left arrows) and the precipitable water vapor in the MBL (WVB; right arrows). Symbols outlined in thick black indicate values that are statistically significant at the 95% confidence level.

necessary for this ecosystem and the increase in the radiation level are important new constraints to be considered in the study of the evolution of the cloud forest in a warmer climate.

4. Conclusions

As pointed out in the IPCC (2013), despite great efforts during the last several decades, our confidence in the sign of the low-cloud feedback still remains low because of the poor representation of low clouds in climate models, diverse model results, and the lack of reliable observational constraints. Nevertheless, both climate models and process models tend to produce positive feedback (IPCC 2013). In this study, the long-term trends of the main characteristics of the MBL that are important to cloud properties in the Atlantic, including the integrated water vapor in both the MBL and the free troposphere, have been analyzed based on radiosonde data for a 30-yr period from 1981 to 2010 at 32 stations distributed from the Azores (~40°N) to

Gough Island (~40°S). To homogenize the IGRA long-term series, the temperature RICH correction and the scheme proposed by Dai et al. (2011) to homogenize humidity were used. The first conclusion is the persistent occurrence of a temperature inversion in the Atlantic, which was detected for 48% of the evaluated radiosondes (202 179 cases out of 417 445). Moreover, the overall changes, with statistical significance, detected in the studied period include an increase in the height of the MBL, a thinning of the temperature inversion layer, and a weakening of the stability. Also, a positive trend in PWV in the MBL (WVB) and a negative trend in the difference between the WVF and WVB (WVD = WVF − WVB) were found for 21 and 12 stations, respectively, with statistical significance. None of the 32 stations showed a negative trend in WVB or a positive trend in WVD with statistical significance. Finally, an overall increase in the static dry stability (LPV) was found at 22 stations, and increases in the moist stabilities were also found although at fewer stations (18 out of 32 stations).
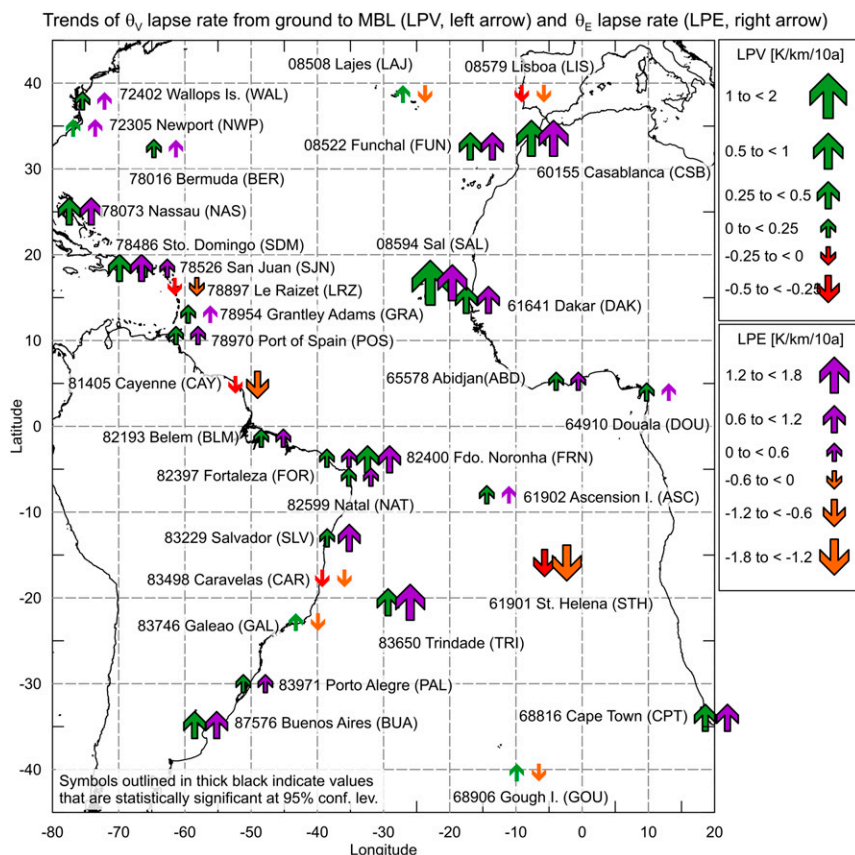
FIG. 7. Trends of the lapse rates of the virtual potential temperature (LPV; left arrows) and the equivalent potential temperature (LPE; right arrows). Symbols outlined in thick black indicate values that are statistically significant at the 95% confidence level.

These results seem to point to a thinning of the low-level cloud layer in a projected warmer climate. Consequently, in addition to the positive cloud-feedback in Earth's energy budget, this possible decrease in the low-cloud cover and in the height of the MBL could also generate possible future adverse changes in the climate conditions that support many current ecosystems, for example, the Macaronesian cloud forests. The results from this study could benefit the climate simulation and projection communities; for example, the environmental conditions responsible for long-term trends found in this study can be used to evaluate and validate the present climate simulations and also for understanding mechanisms and differences among projected future changes in the MBL cloud cover in a warmer climate.

REFERENCES

Bretherton, C. S., and P. N. Blossey, 2014: Low cloud reduction in a greenhouse-warmed climate: Results from Lagrangian LES of a subtropical marine cloudiness transition. *J. Adv. Model. Earth Syst.*, **6**, 91–114, https://doi.org/10.1002/2013MS000250.
——, ——, and C. Jones, 2013: Mechanisms of marine low cloud sensitivity to idealized climate perturbations: A single-LES

exploration extending the CGILS cases. *J. Adv. Model. Earth Syst.*, **5**, 316–337, https://doi.org/10.1002/jame.20019.

Cao, G., T. Giambelluca, D. Stevens, and T. Schroeder, 2007: Inversion variability in the Hawaiian trade wind regime. *J. Climate*, **20**, 1145–1160, https://doi.org/10.1175/JCLI4033.1.

Chan, K. M., and R. Wood, 2013: The seasonal cycle of planetary boundary layer depth determined using COSMIC radio occultation data. *J. Geophys. Res. Atmos.*, **118**, 12 422–12 434, https://doi.org/10.1002/2013JD020147.

Dai, A., J. Wang, P. W. Thorne, D. E. Parker, L. Haimberger, and X. L. Wang, 2011: A new approach to homogenize daily radiosonde humidity data. *J. Climate*, **24**, 965–991, https://doi.org/10.1175/2010JCLI3816.1.

Decker, M., M. Brunke, Z. Wang, K. Sakaguchi, X. Zeng, and M. Bosilovich, 2012: Evaluation of the reanalysis products from GSFC, NCEP, and ECMWF using flux tower observations. *J. Climate*, **25**, 1916–1944, https://doi.org/10.1175/JCLI-D-11-00004.1.

Dee, D. P., and Coauthors, 2011: The ERA-Interim reanalysis: Configuration and performance of the data assimilation system. *Quart. J. Roy. Meteor. Soc.*, **137**, 553–597, https://doi.org/10.1002/qj.828.

Demoto, S., M. Watanabe, and Y. Kamae, 2013: Mechanism of tropical low-cloud response to surface warming using weather and climate simulations. *Geophys. Res. Lett.*, **40**, 2427–2432, https://doi.org/10.1002/grl.50474.

Durre, I., and X. Yin, 2008: Enhanced radiosonde data for studies of vertical structure. *Bull. Amer. Meteor. Soc.*, **89**, 1257–1261, https://doi.org/10.1175/2008BAMS2603.1.

——, R. Vose, and D. Wuertz, 2006: Overview of the Integrated Global Radiosonde Archive. *J. Climate*, **19**, 53–68, https://doi.org/10.1175/JCLI3594.1.

——, ——, and ——, 2008: Robust automated quality assurance of radiosonde temperatures. *J. Appl. Meteor.*, **47**, 2081–2095, https://doi.org/10.1175/2008JAMC1809.1.

Expósito, F. J., A. González, J. C. Pérez, J. P. Díaz, and D. Taima, 2015: High-resolution future projections of temperature and precipitation in the Canary Islands. *J. Climate*, **28**, 7846–7856, https://doi.org/10.1175/JCLI-D-15-0030.1.

Feeley, K. J., and Coauthors, 2011: Upslope migration of Andean trees. *J. Biogeogr.*, **38**, 783–791, https://doi.org/10.1111/j.1365-2699.2010.02444.x.

Foster, P., 2001: The potential negative impacts of global climate change on tropical montane cloud forests. *Earth-Sci. Rev.*, **55**, 73–106, https://doi.org/10.1016/S0012-8252(01)00056-3.

Frierson, D. M. W., 2006: Robust increases in midlatitude static stability in simulations of global warming. *Geophys. Res. Lett.*, **33**, L24816, https://doi.org/10.1029/2006GL027504.

Haimberger, L., 2007: Homogenization of radiosonde temperature time series using innovation statistics. *J. Climate*, **20**, 1377–1403, https://doi.org/10.1175/JCLI4050.1.

——, C. Tavolato, and S. Sperka, 2008: Toward elimination of the warm bias in historic radiosonde temperature records—Some new results from a comprehensive intercomparison of upper-air data. *J. Climate*, **21**, 4587–4606, https://doi.org/10.1175/2008JCLI1929.1.

——, ——, and ——, 2012: Homogenization of the global radiosonde temperature dataset through combined comparison with reanalysis background series and neighboring stations. *J. Climate*, **25**, 8108–8131, https://doi.org/10.1175/JCLI-D-11-00668.1.

IPCC, 2013: *Climate Change 2013: The Physical Science Basis*. T. F. Stocker et al., Eds., Cambridge University Press, 1535 pp.

Irl, S. D., and Coauthors, 2017: An island view of endemic rarity—Environmental drivers and consequences for nature conservation. *Diversity Distrib.*, **23**, 1132–1142, https://doi.org/10.1111/ddi.12605.

Johnson, R. H., P. E. Ciesielski, and K. A. Hart, 1996: Tropical inversions near the 0°C level. *J. Atmos. Sci.*, **53**, 1838–1855, https://doi.org/10.1175/1520-0469(1996)053<1838:TINTL>2.0.CO;2.

Jump, A. S., T. J. Huang, and C. H. Chou, 2012: Rapid altitudinal migration of mountain plants in Taiwan and its implications for high altitude biodiversity. *Ecography*, **35**, 204–210, https://doi.org/10.1111/j.1600-0587.2011.06984.x.

Klein, S., and D. Hartmann, 1993: The seasonal cycle of low stratiform clouds. *J. Climate*, **6**, 1587–1606, https://doi.org/10.1175/1520-0442(1993)006<1587:TSCOLS>2.0.CO;2.

Lauer, A., K. P. Hamilton, Y. Wang, V. T. Phillips, and R. Bennartz, 2010: The impact of global warming on marine boundary layer clouds over the eastern Pacific—A regional model study. *J. Climate*, **23**, 5844–5863, https://doi.org/10.1175/2010JCLI3666.1.

——, R. Bennartz, K. Hamilton, and Y. Wang, 2012: Modeling the response of subtropical marine boundary layer clouds to global warming: The impact of subgrid-scale precipitation formation. *J. Climate*, **25**, 6610–6626, https://doi.org/10.1175/JCLI-D-11-00623.1.

Longman, R. J., H. F. Diaz, and T. W. Giambelluca, 2015: Sustained increases in lower-tropospheric subsidence over the central tropical North Pacific drive a decline in high-elevation rainfall in Hawaii. *J. Climate*, **28**, 8743–8759, https://doi.org/10.1175/JCLI-D-15-0006.1.

Loope, L. L., and T. W. Giambelluca, 1998: Vulnerability of island tropical montane cloud forests to climate change, with special reference to East Maui, Hawaii. *Climatic Change*, **39**, 503–517, https://doi.org/10.1023/A:1005372118420.

McGrath-Spangler, E. L., and A. S. Denning, 2013: Global seasonal variations of midday planetary boundary layer depth from CALIPSO space-borne lidar. *J. Geophys. Res. Atmos.*, **118**, 1226–1233, https://doi.org/10.1002/jgrd.50198.

Medeiros, B., A. Hall, and B. Stevens, 2005: What controls the mean depth of the PBL? *J. Climate*, **18**, 3157–3172, https://doi.org/10.1175/JCLI3417.1.

Molod, A., H. Salmun, and M. Dempsey, 2015: Estimating planetary boundary layer heights from NOAA Profiler Network wind profiler data. *J. Atmos. Oceanic Technol.*, **32**, 1545–1561, https://doi.org/10.1175/JTECH-D-14-00155.1.

Montgomery, M. C., E. A. Peck, and G. G. Vining, 2012: *Introduction to Linear Regression Analysis*. 5th ed. Wiley, 645 pp.

Myers, T., and J. Norris, 2013: Observational evidence that enhanced subsidence reduces subtropical marine boundary layer cloudiness. *J. Climate*, **26**, 7507–7524, https://doi.org/10.1175/JCLI-D-12-00736.1.

Nam, C., S. Bony, J. Dufresne, and H. Chepfer, 2012: The 'too few, too bright' tropical low-cloud problem in CMIP5 models. *Geophys. Res. Lett.*, **39**, L21801, https://doi.org/10.1029/2012GL053421.

Pouteau, R., T. W. Giambelluca, C. Ah-Peng, and J. Y. Meyer, 2018: Will climate change shift the lower ecotone of tropical montane cloud forests upwards on islands? *J. Biogeogr.*, **45**, 1326–1333, https://doi.org/10.1111/jbi.13228.

Rossow, W. B., and R. A. Schiffer, 1999: Advances in understanding clouds from ISCCP. *Bull. Amer. Meteor. Soc.*, **80**, 2261–2288, https://doi.org/10.1175/1520-0477(1999)080<2261:AIUCFI>2.0.CO;2.

Seidel, D. J., C. O. Ao, and K. Li, 2010: Estimating climatological planetary boundary layer heights from radiosonde

observations: Comparison of methods and uncertainty analysis. *J. Geophys. Res.*, **115**, D16113, https://doi.org/10.1029/2009JD013680.

Sherwood, S., S. Bony, and J. Dufresne, 2014: Spread in model climate sensitivity traced to atmospheric convective mixing. *Nature*, **505**, 37–42, https://doi.org/10.1038/nature12829.

Slingo, J. M., 1987: The development and verification of a cloud prediction scheme for the ECMWF model. *Quart. J. Roy. Meteor. Soc.*, **113**, 899–927, https://doi.org/10.1002/qj.49711347710.

Sperling, F. N., R. Washington, and R. J. Whittaker, 2004: Future climate change of the subtropical North Atlantic: Implications for the cloud forests of Tenerife. *Climatic Change*, **65**, 103–123, https://doi.org/10.1023/B:CLIM.0000037488.33377.bf.

Torrence, C., and G. P. Compo, 1998: A practical guide to wavelet analysis. *Bull. Amer. Meteor. Soc.*, **79**, 61–78, https://doi.org/10.1175/1520-0477(1998)079<0061:APGTWA>2.0.CO;2.

von Engeln, A., and J. Teixeira, 2013: A planetary boundary layer height climatology derived from ECMWF reanalysis data. *J. Climate*, **26**, 6575–6590, https://doi.org/10.1175/JCLI-D-12-00385.1.

Wang, J., L. Zhang, A. Dai, F. Immler, M. Sommer, and H. Vömel, 2013: Radiation dry bias correction of Vaisala RS92 humidity data and its impacts on historical radiosonde data. *J. Atmos. Oceanic Technol.*, **30**, 197–214, https://doi.org/10.1175/JTECH-D-12-00113.1.

——, A. Dai, and C. Mears, 2016: Global water vapor trend and its diurnal asymmetry based on GPS, radiosonde and microwave satellite measurements. *J. Climate*, **29**, 5205–5222, https://doi.org/10.1175/JCLI-D-15-0485.1.

Wang, L., Y. Wang, A. Lauer, and S.-P. Xie, 2011: Simulation of seasonal variation of marine boundary layer clouds over the eastern Pacific with a regional climate model. *J. Climate*, **24**, 3190–3210, https://doi.org/10.1175/2010JCLI3935.1.

Wang, X. Y., and K. C. Wang, 2014: Estimation of atmospheric mixing layer height from radiosonde. *Atmos. Meas. Tech.*, **7**, 1701–1709, https://doi.org/10.5194/amt-7-1701-2014.

Wang, Y., S.-P. Xie, H. Xu, and B. Wang, 2004a: Regional model simulations of marine boundary layer clouds over the southeast Pacific off South America. Part I: Control experiment. *Mon. Wea. Rev.*, **132**, 274–296, https://doi.org/10.1175/1520-0493(2004)132<0274:RMSOMB>2.0.CO;2.

——, H. Xu, and S.-P. Xie, 2004b: Regional model simulations of marine boundary layer clouds over the southeast Pacific off South America. Part II: Sensitivity experiments. *Mon. Wea. Rev.*, **132**, 2650–2668, https://doi.org/10.1175/MWR2812.1.

——, S.-P. Xie, B. Wang, and H. Xu, 2005: Large-scale atmospheric forcing by southeast Pacific boundary layer clouds: A regional model study. *J. Climate*, **18**, 934–951, https://doi.org/10.1175/JCLI3302.1.

Wood, R., 2012: Stratocumulus clouds. *Mon. Wea. Rev.*, **140**, 2373–2423, https://doi.org/10.1175/MWR-D-11-00121.1.

——, and C. Bretherton, 2006: On the relationship between stratiform low cloud cover and lower-tropospheric stability. *J. Climate*, **19**, 6425–6432, https://doi.org/10.1175/JCLI3988.1.

Zhang, C.-X., Y. Wang, and K. Hamilton, 2011: Improved representation of boundary layer clouds over the southeast Pacific in WRF-ARW using a modified Tiedtke cumulus parameterization scheme. *Mon. Wea. Rev.*, **139**, 3489–3513, https://doi.org/10.1175/MWR-D-10-05091.1.

——, ——, A. Lauer, K. Hamilton, and F. Xie, 2012: Cloud base and top heights in the Hawaiian region determined by satellite and ground-based measurements. *Geophys. Res. Lett.*, **39**, L15706, https://doi.org/10.1029/2012GL052355.

——, ——, K. Hamilton, and A. Lauer, 2016a: Dynamical downscaling of the climate for the Hawaiian Islands. Part I: Present day. *J. Climate*, **29**, 3027–3048, https://doi.org/10.1175/JCLI-D-15-0432.1.

——, ——, ——, and ——, 2016b: Dynamical downscaling of the climate for the Hawaiian Islands. Part II: Projection for the late twenty-first century. *J. Climate*, **29**, 8333–8354, https://doi.org/10.1175/JCLI-D-16-0038.1.

Zhang, M., and Coauthors, 2013: CGILS: Results from the first phase of an international project to understand the physical mechanisms of low cloud feedbacks in single column models. *J. Adv. Model. Earth Syst.*, **5**, 826–842, https://doi.org/10.1002/2013MS000246.

Zhang, Y. H., D. J. Seidel, and S. Zhang, 2013: Trends in planetary boundary layer height over Europe. *J. Climate*, **26**, 10 071–10 076, https://doi.org/10.1175/JCLI-D-13-00108.1.

Zhang, Y. Y., B. Stevens, B. Medeiros, and M. Ghil, 2009: Low-cloud fraction, lower-tropospheric stability, and large-scale divergence. *J. Climate*, **22**, 4827–4844, https://doi.org/10.1175/2009JCLI2891.1.